FtsZ treadmilling is essential for Z-ring condensation and septal constriction initiation in *Bacillus subtilis* cell division

Kevin D. Whitley[1,2+], Calum Jukes[1+], Nicholas Tregidgo[1], Eleni Karinou[1], Pedro Almada[3], Ricardo Henriques[3], Cees Dekker[2], and Séamus Holden[1*]

[1]Centre for Bacterial Cell Biology, Biosciences Institute, Faculty of Medical Sciences, Newcastle University, Newcastle upon Tyne, UK; [2]Department of Bionanoscience, Kavli Institute of Nanoscience Delft, Delft University of Technology, Delft, The Netherlands; [3]MRC-Laboratory for Molecular Cell Biology, University College London, London, UK

*Corresponding author: seamus.holden@ncl.ac.uk

+Equal author contribution

ABSTRACT

Despite the central role of division in bacterial physiology, how division proteins work together as a nanoscale machine to divide the cell remains poorly understood. Cell division by cell wall synthesis proteins is guided by the cytoskeleton protein FtsZ, which assembles at mid-cell as a dense Z-ring formed of treadmilling filaments[1,2]. However, although FtsZ treadmilling is essential for cell division, the function of FtsZ treadmilling remains unclear[2–5]. Here, we systematically resolve the function of FtsZ treadmilling across each stage of division in the Gram-positive model organism *Bacillus subtilis* using a novel combination of nanofabrication, advanced microscopy, and microfluidics to measure the division-protein dynamics in live cells with ultrahigh sensitivity. We find that FtsZ treadmilling has two essential functions: mediating condensation of diffuse FtsZ filaments into a dense Z-ring, and initiating constriction by guiding septal cell wall synthesis. After constriction initiation, FtsZ treadmilling has a dispensable function in accelerating septal constriction rate. Our results show that FtsZ treadmilling is critical for assembling and initiating the bacterial cell division machine.

INTRODUCTION

Bacterial cell division is an essential cellular process and a key target for antibiotics. Bacterial cell division is also a remarkable feat of molecular self-assembly where a nanoscale divisome machine builds a micron-scale wall (septum) at mid-cell. The core components of this machine include the septal cell-wall synthases that insert new peptidoglycan (PG) to build the septum, and the essential cytoskeletal tubulin homologue FtsZ that polymerises into a dense "Z-ring" band of short filaments at mid-cell[6–8]. These short FtsZ filaments move by treadmilling, a type of motion where an asymmetric filament undergoes plus-end polymerisation and minus-end depolymerisation, with GTP hydrolysis setting the rate of FtsZ depolymerisation and overall treadmilling speed[1,2,9]. FtsZ treadmilling dynamics are essential for cell division[2–5].

However, the role of FtsZ treadmilling in cell division remains unclear. In the Gram-positive model organism *Bacillus subtilis*, we previously observed that constriction rate and synthase speed was dependent upon FtsZ filament speed[1], leading to an initial model of a tightly coupled motile cytoskeleton-synthase complex, where FtsZ acts an obligatory guide and rate-limiting step for septal PG synthesis. In contrast, FtsZ treadmilling is dispensable after constriction initiation in *Staphylococcus aureus*[3], even though the two organisms belong to the same phylogenetic class. This could reflect genuine differences between species, or there may exist a common division mechanism where FtsZ treadmilling plays different roles at different division stages. To date, it remains unclear how the role of treadmilling FtsZ filaments varies across the full division process.

Here, we measure the dynamics and function of FtsZ treadmilling across all division stages in *B. subtilis*. To make these observations, we developed a new method combining nanofabrication, advanced microscopy, and microfluidics. This approach allowed us to measure native FtsZ dynamics at near-single-filament resolution throughout division. We found that treadmilling dynamics drive FtsZ filament interactions during Z-ring assembly and that this stabilises filaments into dense Z-rings. We determined that the FtsZ inhibitor PC190723 arrests FtsZ treadmilling within seconds, independent of division stage, allowing us to elucidate the rapid response of cells to treadmilling arrest. By systematically determining the response of single cells to FtsZ treadmilling arrest by PC190723, we found that FtsZ treadmilling has two separate essential functions: mediating Z-ring assembly during the earliest stage of cell division, and subsequently for guiding septal constriction initiation. We found that FtsZ treadmilling becomes dispensable after constriction initiation but increases septal constriction rate, reconciling the findings from previous studies[1,3]. Our results show that the key roles of FtsZ treadmilling are to drive Z-ring assembly and to initiate septal constriction.

RESULTS

FtsZ assembly at mid-cell has three distinct phases: nascent, mature, and constricting Z-rings

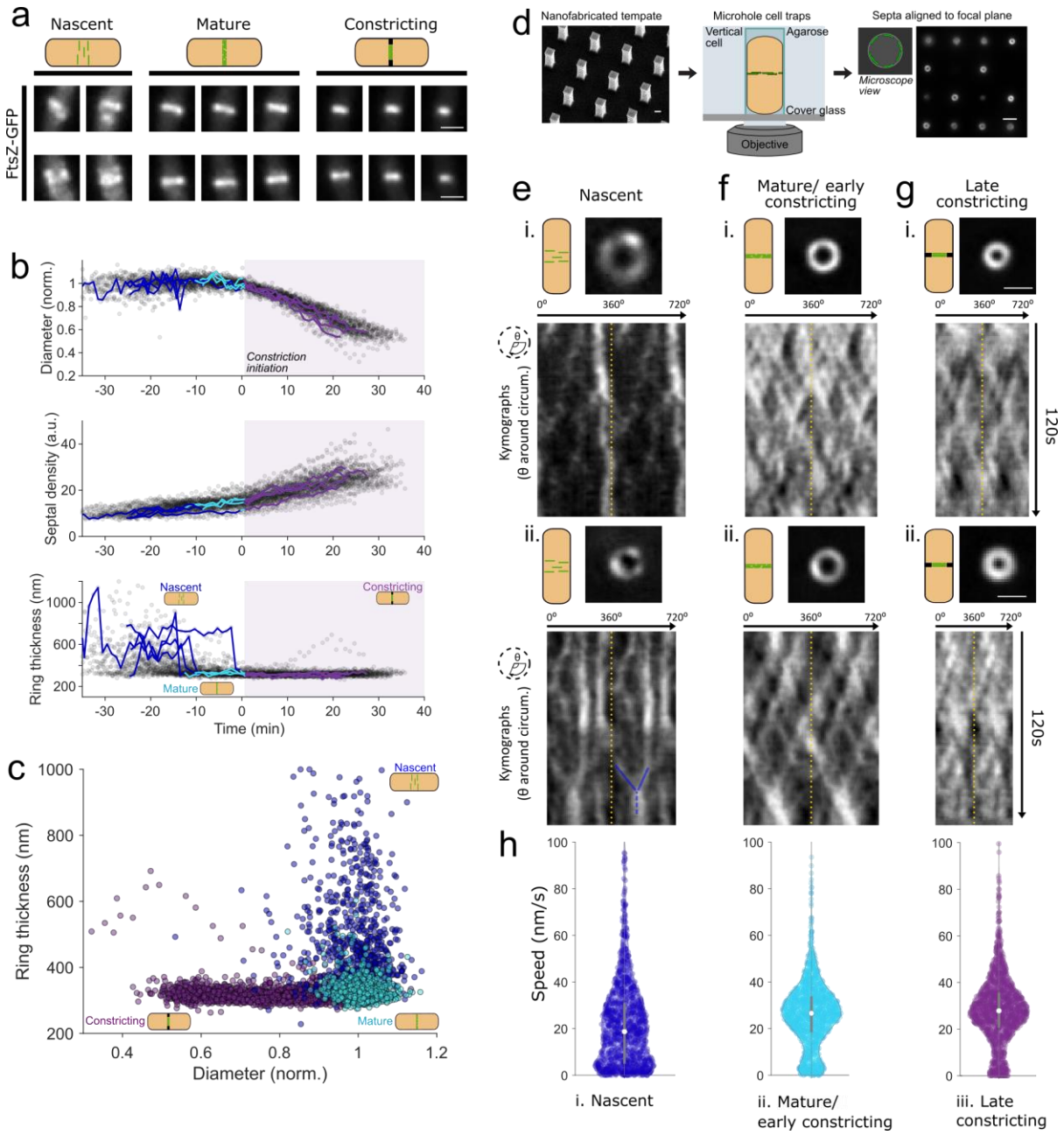

Figure 1. FtsZ filament organisation and dynamics throughout the division process. *(a) Exemplar images of FtsZ-GFP (SH130) filament organisation throughout division, classified by division phase. (b) Quantification of FtsZ-ring diameter, ring thickness and septal density (septal intensity divided by ring circumference) throughout division from time-lapse microscopy data*. Nascent Z-rings have large axial width (ring thickness) due to the diffuse distribution of filaments, which condense into a thin mature Z-ring, followed by constriction initiation. Traces are temporally aligned relative to the start time of constriction (Methods). Grey scatter points represent all data points. Lines show individual, representative traces, which are split into coloured segments indicating cell division state: nascent (blue), mature (cyan), and constricting (purple). *(c) FtsZ-ring thickness and relative septal diameter.* Colour indicates cell division state as per (b). Cell division state of FtsZ-rings in (b-c) determined by automated classification of Z-ring diameter and axial thickness time lapse data (Methods, SI Note 3). *(d) VerCINI schematic.* Rod-shaped bacteria are trapped in agarose microholes, rotating the division septum into microscope imaging plane. *(e-g) VerCINI microscopy of FtsZ filament dynamics for each Z-ring phase, two representative examples per phase (i-ii)*. Nascent Z-rings are composed of sparse filaments diffusely distributed around the circumference of the cell, and a large fraction of immobile FtsZ filaments. Mature and constricting Z-rings possess a more uniform distribution of FtsZ filaments around the division site, with most filaments treadmilling. Images of septa show the first frame in kymographs (t=0 s). Kymographs were obtained by fitting septal images to circles and plotting intensity values around the circumference of

the cell for each frame of the time-lapse (1 frame/ s). Two full revolutions around the cell (0-720°) are plotted side-by-side in each kymograph to resolve filament trajectories that pass 0°/360°, separated by yellow dotted lines. Blue lines highlight example of motile FtsZ filament aggregation. *(h) Violin plots of FtsZ filament speed for each Z-ring phase.* White circles, median; thick grey lines, interquartile range; thin grey lines, 1.5x interquartile range.

We first determined FtsZ organisation during cell division in *B. subtilis* using an FtsZ-GFP fusion[10] expressed from the native locus at near wild-type protein levels (SH130, Methods, Supplementary Figure 1). Cell morphology analysis showed near native morphology with only a mild elongation phenotype at both 30°C and 37°C (Supplementary Figure 2), although growth in liquid culture was not impaired at either temperature (Supplementary Figure 3).

We performed time-lapse imaging of FtsZ-GFP organisation in slow growth conditions (Figure 1; Supplementary Video 1). We observed that FtsZ filaments initially formed a diffuse structure at mid-cell which rapidly condensed into a dense narrow band, followed by the onset of constriction (Figure 1a). We quantified these changes in Z-ring structure by measuring the dimensions (thicknesses and diameters) and septal density (total septal intensity divided by Z-ring circumference) of the Z-rings in each frame (Methods). The resulting traces of thicknesses and diameters over time were aligned by the start time of constriction (Methods, Figure 1b). These time traces revealed three distinct Z-ring stages that we classified as 'nascent', 'mature', and 'constricting' based on Z-ring diameter and axial thickness (Figure 1b, Methods, Supplementary Note 3). During the nascent Z-ring stage, low density FtsZ filaments transiently assemble at mid-cell over a wide region, consistent with previous reports[4,13–15]. FtsZ filaments then rapidly condense into a thin mature Z-ring structure, which remains unconstricted but increases in intensity for some time. Finally, the Z-ring begins constricting until division is finished. Step finding analysis of Z-ring axial thickness time traces showed that Z-ring condensation occurs rapidly and stochastically approximately 10 minutes before constriction initiation (Figure 1b, Methods, Supplementary Figure 4).

VerCINI microscopy reveals FtsZ filament dynamics are division stage regulated and FtsZ treadmilling drives filament encounter in nascent Z-rings

FtsZ filament dynamics are difficult to observe *in vivo*. TIRF imaging only illuminates a thin slice of the septum, limiting observation to partial snapshots of filament dynamics in nascent Z-rings[1,2]. We previously developed a prototype approach which resolves this problem by vertically immobilizing cells in nanofabricated chambers, allowing continuous imaging of the entire division septum, including dense actively constricting Z-rings[1,4]. However, the prototype method was not capable of imaging dim, nascent Z-rings due to high background, suffered from fast photobleaching and lacked the throughput required.

We created an entirely redesigned vertical cell immobilisation method which addresses all of these issues and allows ultrasensitive high-resolution imaging of FtsZ filament dynamics at all stages of division, termed VerCINI (Vertical Cell Imaging by Nanostructured Immobilisation). This new method features a high-throughput chip design, centrifugation loading, high SNR ring-HiLO illumination[16], imaging denoising[17], and custom septal localisation and background subtraction algorithms (Methods, Supplementary Figure 5-6, Supplementary Videos 2-3). We measured FtsZ filament dynamics during each division stage using VerCINI (Figure 1e-h, Supplementary Figure 7, Supplementary Videos 4-6)[1,21]. Division stage was determined based on septal intensity and diameter (Methods, Supplementary Figure 8, Supplementary Note 3).

In nascent Z-rings, we observed that FtsZ filaments are sparsely distributed, with a mixture of treadmilling and immobile filaments (Figure 1f, Supplementary Figure 9a, 35% immobile, filament speed < 10 nm/s), leading to a low average filament speed with large spread (median 19 nm/s, interquartile range, IQR, 5-31, N=526). Surprisingly, we frequently observed two or more treadmilling

FtsZ filaments colliding, often leading to aggregation and temporary arrest of both filaments (Figure 1eii, Supplementary Figure 7). FtsZ filament aggregation by lateral filament interactions is required to bundle FtsZ filaments and condense the Z-ring[22–26]. These data show that FtsZ treadmilling can drive filament aggregation by promoting the filament encounters required for lateral interactions.

Z-ring condensation led to a drop in the number of immobile FtsZ filaments in mature/early constricting Z-rings, yielding a significant increase in average filament speed with narrower speed distribution (15% immobile, median 27 nm/s, IQR 19-34, N=1053; Figure 1h). Simulations showed that changes in filament density had little effect on observed filaments speeds or observed fraction of immobile FtsZ filaments (Supplementary Figure 10, Supplementary Note 4). Filament speeds in late constricting Z-rings were similar to those of mature/early constricting Z-rings (13% immobile, median speed 28 nm/s, IQR 21-36, N=1677; Figure 1h). Due to the decreased immobile population, filaments in mature and constricting Z-rings traversed, on average, twice the distance around the septum of those in nascent rings (Supplementary Figure 9c). Furthermore, we found that treadmilling and immobile filaments displayed similar lifetimes (Supplementary Figure 11), suggesting that immobile filaments are dynamic. These results show that the fraction of treadmilling FtsZ filaments and their speeds are division stage regulated.

PC190723 arrests FtsZ treadmilling within seconds throughout division

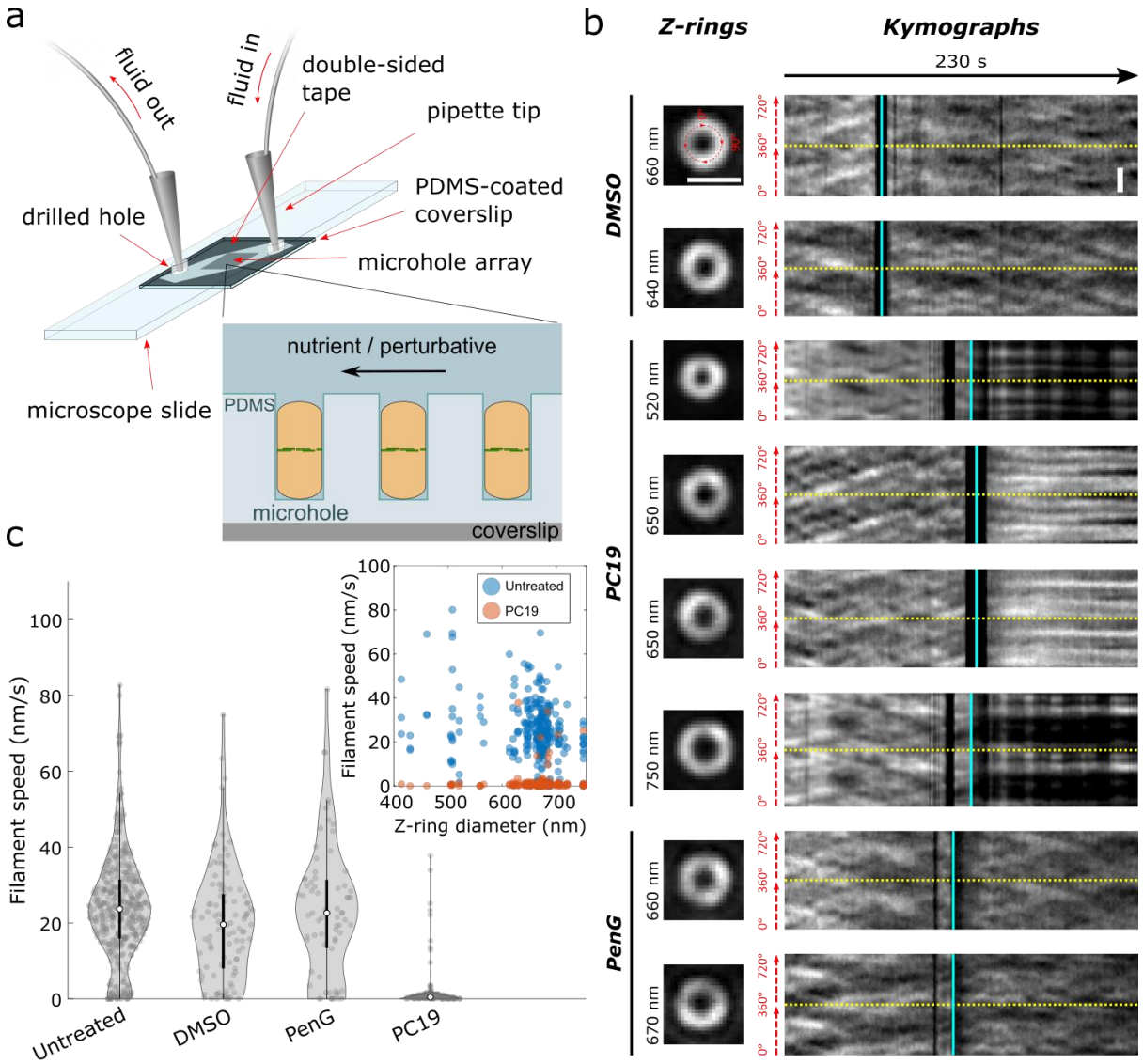

Figure 2. PC190723 arrests cellular FtsZ treadmilling within seconds across all stages of constriction. *(a) Schematic of microfluidic VerCINI.* Rod-shaped cells are confined in open-topped microholes in a thin layer of PDMS atop a microscope coverslip as solutions flow over them. The flow channel is formed from a cut piece of double-sided tape sandwiched between the PDMS layer and a microscope cover slide with drilled holes to allow inlet and outlet tubes. *(b) Representative images of septa and associated kymographs of FtsZ-GFP (SH130) dynamics in vertically-immobilised cells during rapid treatment with either DMSO (top), PC19 (middle), or PenG (bottom) at multiple septal diameters.* Images of septa show the first frame in kymographs (t=0 s). Kymographs were obtained by fitting septal images to circles and plotting intensity values around the circumference of the cell for each frame of the time-lapse (1 frame/s). Two full revolutions around the cell (0-720°) are plotted side-by-side in each kymograph to resolve filament trajectories that pass 0°/360°, separated by yellow dotted lines. Cyan lines show arrival time of media containing DMSO, PenG, or PC19. Black bands around time of treatment resulted from a loss of focus during fluid exchange. Fluctuations in intensity for two septa post-PC19 treatment (750 nm and 520 nm diameter septa) resulted from manual refocusing during imaging. Scale bars: 1000 nm. *(c) Violin plots of FtsZ treadmilling speeds pre- and post-treatment measured from kymographs.* White circles, median; thick black lines, interquartile range; thin black lines, 1.5x interquartile range. DABEST plots of effect size can be found in Supplementary Figure 12. *Inset:* FtsZ treadmilling speed distributions for untreated (white circles) and PC19-treated (red circles) cells from violin plots separated by septal diameter.

We next set out to determine the function of FtsZ treadmilling during each stage of cell division. For this we needed to observe the effect on cell division in response to rapid FtsZ treadmilling arrest. The antibiotic PC190723 (PC19) arrests FtsZ treadmilling in *B. subtilis* and related species by supporting the 'open' conformation of FtsZ and stabilizing protofilaments[1,18–21] without fully abolishing subunit turnover or GTPase activity[22]. Since the entire cell division process takes only 10-20 minutes in fast

growth conditions, it was critical to determine whether PC19 acted sufficiently rapidly and robustly for use in dissecting the effect of treadmilling during each division stage. To determine how PC19 and other cell division inhibitors perturb FtsZ treadmilling, we developed microfluidic VerCINI, which combines high-resolution imaging of cell division protein dynamics *in vivo* with rapid chemical perturbation (Methods, Figure 2a). In this method, cells are confined in an array of open-topped microholes formed from PDMS atop a microscope coverslip, which is contained within a microfluidic chamber to allow continual flow of fresh media as well as chemical inhibitors. PDMS was used rather than agarose in order to produce a thin enough layer (~50 µm) to image through. Cells continued to grow and divide, consistent with previous observations that growth of *B. subtilis* cells in sufficiently wide (>0.8 µm) PDMS channels is not impaired[23], and models demonstrating that nutrient transport does not significantly limit growth in short (<20 µm) channels[24]. A real-time image-based autofocus system was used to stabilise focus during high-speed imaging[25].

We imaged FtsZ-GFP (SH130) using microfluidic VerCINI to observe the effects of division inhibitors PC19 and Penicillin G (PenG) on FtsZ treadmilling. We recorded untreated FtsZ dynamics for 90 s while blank media flowed over the cells, then continuously treated cells with an excess of division inhibitor by changing fluid flow to media laced with the compound (Figure 2b, Supplementary Video 7). FtsZ treadmilling dynamics were abolished by PC19 within a few seconds for all diameters of septa observed (Figure 2c). When we treated cells with Penicillin G (PenG), which inhibits cell wall synthesis by binding to cell wall synthase transpeptidation sites, FtsZ dynamics continued unperturbed for the duration of the experiment (several minutes). FtsZ dynamics were also unaffected by a DMSO-only control, the solvent for PC19 (Figure 2c, Supplementary Videos 8-9).

By providing high spatiotemporal resolution during rapid chemical perturbation, microfluidic VerCINI revealed the effect of division inhibitors on FtsZ treadmilling throughout division. Our results demonstrate that PC19 inhibits FtsZ treadmilling within seconds well after the start of constriction, whereas PenG treatment does not directly affect FtsZ dynamics.

188 **FtsZ treadmilling is essential for Z-ring condensation and septal constriction initiation, but is**
189 **subsequently dispensable**

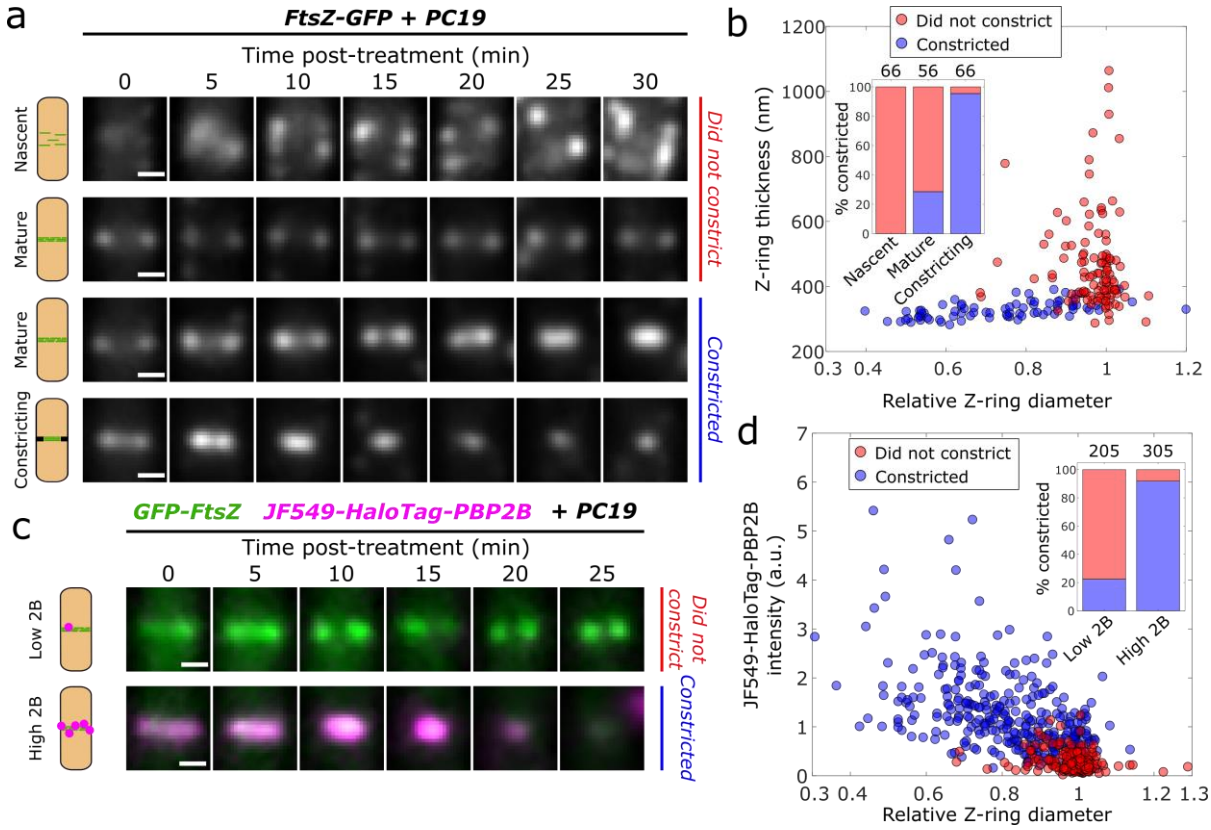

190

191 **Figure 3. FtsZ treadmilling is required until the arrival of PG synthesis machinery.** *(a) Representative time-lapses of Z-rings*
192 *for FtsZ-GFP cells (SH130) after arrival of 10 µM PC19-laced media.* Nascent rings and many mature rings do not constrict for
193 tens of minutes after PC19 treatment, whereas constricting rings and many mature rings continue constricting after
194 treatment. *(b) Scatter plot of Z-ring diameters and thicknesses for all FtsZ-GFP cells at t=0 min showing whether they*
195 *continued constricting (blue) or not (red). Inset*: Percentage of cells that continued constricting classified by division stage.
196 Nascent: thickness>400 nm, mature: thickness<400 nm, relative diameter>0.9, constricting: thickness<400 nm, relative
197 diameter<0.9. *(c) Representative time-lapses of rings from two-colour strain SH212 (Green: GFP-FtsZ, magenta: JF549-*
198 *HaloTag-PBP2B) after the arrival of PC19-laced media.* Z-rings with low HT-PBP2B signal typically do not continue constricting
199 while those with high signal typically do. *(d) Scatter plot of Z-ring diameters and normalised HT-PBP2B intensities for mature*
200 *Z-rings only at t=0 min showing whether they continued constricting (blue) or not (red). Inset:* Percentage of cells that
201 continued constricting classified by JF549-HaloTag-PBP2B signal. Low 2B: intensity<0.5, high 2B: intensity>0.5. Scale bars:
202 500 nm. Numbers above stacked bars indicate number of cells.

203 We used PC19 to investigate the role of FtsZ treadmilling throughout cell division. We imaged cells in
204 fast growth conditions (rich media, 37°C) using a commercial microfluidic device with continual fluid
205 flow both before and during treatment with excess PC19 (Figure 3, Methods). Treatment with PC19
206 prevented Z-rings in earlier stages of division from continuing to divide, but Z-rings in later stages
207 continued dividing (Figure 3a-b, Supplementary Videos 10-13). PC19 treatment prevented 96% (N=62)
208 of nascent Z-rings from condensing into mature Z-rings (Supplementary Figure 13) and 100% (N=66)
209 from constricting (Figure 3b). Furthermore, we found that treatment prevented 71% (N=56) of mature
210 Z-rings from beginning constriction, while only 5% (N=66) of initially constricting Z-rings were
211 prevented from continuing constriction. In contrast, treatment with PenG inhibited constriction
212 altogether (Supplementary Video 14). Similar results were observed in slow growth conditions (poor
213 media, 30°C; Supplementary Figure 14, Supplementary Video 15). Together these data suggest that
214 FtsZ treadmilling is required for the condensation of filaments from a nascent to a mature Z-ring, but
215 becomes dispensable at some point during the mature Z-ring stage.

It is worth noting that PC19 also affects FtsZ GTPase activity and filament structure[18]. These are likely downstream effects of the primary mode of action, which is to stabilize the polymeric state of the protein. We note that FtsZ retains ~25% GTPase activity even with excess PC19[18]. Furthermore, in cells treated with 8j (a relative of PC19) the subunits in immobile FtsZ foci still turn over slowly[22], which suggests filaments are still dynamic despite not treadmilling. So, while we cannot strictly rule out the possibility that our observations result from a downstream effect of PC19, we believe the most parsimonious explanation for our results is that the arrest of treadmilling specifically is responsible.

We considered whether these effects were specific to PC19 by repeating the assay with the non-benzamide FtsZ inhibitor PC58538 (PC58). This compound inhibits FtsZ by a separate mode of action from PC19: Rather than stabilizing protofilaments, it prevents filament assembly[26]. As with PC19, PC58 prevented 84% (N=50) of nascent Z-rings from condensing into mature Z-rings and 90% (N=50) from constricting, but prevented 60% (N=52) of mature and only 6% (N=33) of constricting Z-rings from constricting (Supplementary Figure 15, Supplementary Video 16). Interestingly, similar results were recently demonstrated using ADEP antibiotics, which activate the protease ClpP to degrade FtsZ monomers and thereby deplete the cytoplasmic pool needed for filament assembly[27]. We also repeated the above experiment with exogenous addition of *B. subtilis* MciZ, although we found that the timescale of action was too slow draw conclusions about its effect on Z-ring condensation or constriction (data not shown). We conclude that arresting FtsZ treadmilling with PC19 produces an effect similar to, and as severe as, preventing FtsZ filament assembly altogether, emphasizing the critical role of FtsZ treadmilling in cell division initiation.

To further investigate the role of FtsZ treadmilling in Z-ring condensation, we examined the effect of an FtsZ mutant that is deficient in GTP hydrolysis. The mutant FtsZ(D212A) in *E. coli* was shown to have greatly reduced GTPase activity[28,29], and exogenous expression of the equivalent FtsZ(D213A) mutant in *B. subtilis* reduces FtsZ treadmilling speed[1] (Supplementary Figure 16). We constructed a merodiploid strain expressing FtsZ-GFP from the native locus and FtsZ(D213A) from a secondary locus under an IPTG-inducible promoter (SH131, Methods). For comparison to wild-type (Figure 1) we imaged this strain under slow growth conditions (poor media, 30°C) with an induction level (10 µM IPTG) that supported growth in liquid culture (Supplementary Figure 3) and cell division (Supplementary Video 17). Condensation of nascent Z-rings was significantly perturbed under these conditions: 54% (N=74) of nascent Z-rings failed to fully condense into narrow Z-rings prior to constriction initiation, and even throughout constriction Z-rings remained 65 nm (95% CI [63,67]) thicker than wild-type (Supplementary Figure 17), consistent with previous measurements in *E. coli*[30]. This partial Z-ring condensation phenotype is consistent with partial inhibition of FtsZ treadmilling caused by expression of the GTPase-deficient mutant.

We investigated how FtsZ(D213A)-expressing cells could still constrict despite forming thick partially condensed Z-rings. First, we performed state detection on the D213A Z-rings to attempt to identify transitions between a nascent and condensed state. However, unlike in wild type cells, we could only reliably detect a single pre-constricted Z-ring state in the D213A cells (Supplementary Figure 18a-b). We thus compared the axial thickness of the D213A Z-rings to that of WT nascent and mature Z-rings. We found that the thickness of the D213A Z-rings is intermediate between that of WT nascent and mature Z-rings. We also noticed that most pre-constricted D213A Z-rings looked quite dissimilar to the highly dynamic, non-condensed structures characteristic of the nascent division stage in wild-type cells, but more like stable, condensed mature Z-rings except with aberrant shapes (Supplementary Videos 1 and 17). This prompted us to measure the variation in Z-ring axial thickness over time for both wild type and D213A-expressing cells. We found that the variations in thickness for pre-constricted mutant Z-ring structures were small and comparable to those of mature wild-type Z-rings (Supplementary Figure 18d). On the other hand, the axial thickness of nascent Z-rings in wild-type cells

263 was highly variable, consistent with their visibly dynamic appearance, and was considerably move
264 variable than either wild-type mature Z-rings or FtsZ(D213A) pre-constricted Z-rings (Supplementary
265 Figure 18c). Taken together these results show that in cells expressing GTPase-deficient FtsZ(D213A),
266 FtsZ filaments rapidly aggregate into partially condensed Z-rings which are dense and structurally
267 stable, but which have increased axial thickness compared to mature Z-rings in wild-type cells.

268 To further investigate the connection between condensation and septal constriction, we imaged wild-
269 type and D213A-expressing cells with a membrane stain (Supplementary Figure 18e). In the mutant,
270 we observed sharp membrane invaginations in many cases where aberrant Z-ring shapes occurred,
271 indicating active but aberrant constriction. In contrast, we did not observe any clear cases of
272 membrane invagination over areas corresponding to nascent Z-rings in wild-type cells. These
273 observations indicate that the rapid treadmilling dynamics of FtsZ filaments in wild-type nascent Z-
274 rings are likely required to form a compact Z-ring structure to mark the division septum to enable
275 constriction. Reduced filament treadmilling and turnover in the FtsZ(D213A) mutant still allow
276 assembly of a dense Z-ring structure, but locked into a thick, partially-condensed state that is less
277 effective in directing cell division. This observation is reminiscent of how dynamic instability of
278 microtubules allows them to rapidly conform to the complex intracellular geometry of eukaryotic cells.

279 We next wondered what events within the mature Z-ring stage corresponded to the change in
280 dispensability of FtsZ treadmilling. Divisome assembly in *B. subtilis* is approximately a two-step process
281 where FtsZ and other cytoplasmic proteins arrive first, followed by arrival of the PG synthesis
282 machinery just before constriction initiation, including the septal transpeptidase PBP2B[31]. To
283 determine when FtsZ treadmilling becomes dispensable within mature Z-rings, we repeated the
284 treadmilling inhibition assay using a 2-colour strain where FtsZ and PBP2B are both labelled. Since
285 fully-labelled FtsZ slightly perturbed cell physiology (Supplementary Figure 2) and full labelling of FtsZ
286 was unnecessary for this assay, for the labelled FtsZ we decided to use a well-characterized
287 merodiploid harbouring an N-terminal GFP-FtsZ fusion[22] that could be expressed at a low non-
288 perturbative level. We therefore constructed a 2-colour strain (SH212, Methods) expressing GFP-FtsZ
289 from an ectopic locus and HaloTag-PBP2B from its native locus. To quantify the amount of PBP2B at
290 septa, we labelled HaloTag-PBP2B with an excess of JF549 HaloTag ligand[32] (Methods). This strain
291 showed the same response overall to PC19 treatment as before (Supplementary Figure 19,
292 Supplementary Videos 18-19). For mature rings we found that the amount of PBP2B present at time
293 of FtsZ treadmilling arrest correlated strongly with whether rings would constrict or not (Figure 3c-d).
294 Similar results were obtained for a functional mNeonGreen-PBP2B fusion expressed from the native
295 locus[1] (ME7 Supplementary Video 20, Supplementary Figure 20). The GFP-FtsZ signal also increased
296 during the mature ring stage, but unlike PBP2B the FtsZ signal was only weakly correlated with the
297 percentage of cells continuing constriction (Supplementary Figure 19b). FtsZ treadmilling thus
298 becomes dispensable for cell division just after the arrival of the PG synthesis machinery. These results
299 are consistent with previous findings in *S. aureus* that FtsZ treadmilling is required until constriction
300 has initiated, and thereafter becomes dispensable[3]. Since we previously observed that FtsZ
301 treadmilling guides processive PG synthesis around the septum[1], we conclude that FtsZ treadmilling
302 in mature Z-rings likely functions by guiding the processive motion of septal synthases during the
303 earliest stages of septal synthesis, before a septum has been formed.

304 Together, our data reveal two essential functions for FtsZ treadmilling in division. The first is a novel
305 peptidoglycan synthesis-independent function, to condense sparse FtsZ filaments into a dense Z-ring.
306 The second function is to initiate constriction by guiding initial cell-wall synthesis.

307 **FtsZ treadmilling accelerates constriction**

308 We wondered how to reconcile the finding that FtsZ treadmilling is dispensable for constriction after
309 initiation, with our previous observation that FtsZ treadmilling sets the rate of constriction[1]. To
310 address this, we set out to determine the effect of rapid, total arrest of FtsZ treadmilling on the septal
311 constriction rate using natively-expressed mNeonGreen-PBP2B as a septal marker (strain ME7). In
312 order to precisely measure constriction rates immediately after PC19 treatment, we developed a
313 physical model for Gram-positive septal constriction which could be fitted to partial septal constriction
314 trajectories immediately after cell treatment with PC19 (Methods, Supplementary Note 2, Figure 4a).
315 For comparison to previous observations we converted the observed constriction rates of partially
316 constricted cells to an effective constriction time t_{eff}, the total amount of time it would take for an
317 average septum to constrict completely (Methods).

318 We observed that the constriction time of untreated cells in fast growth conditions was 15.3 min, IQR
319 13.5-17.9 (N=765, Figure 4b). FtsZ treadmilling inhibition by PC19 treatment caused a robust 7.7 min,
320 95% CI [6.9,8.3] (N=419), increase in constriction time for cells grown in rich media. This is similar to
321 the increase in constriction time caused by high expression of the GTP-hydrolysis-impaired
322 FtsZ(D213A) mutant (Supplementary Figure 21). Fluorescent PBP2B signal continued to increase after
323 treatment with PC19 (Supplementary Figure 22), indicating that the reduced constriction rate is
324 unlikely to be caused by indirect reduction of synthase levels at the septum. These results show that
325 although FtsZ treadmilling is not required for septal PG synthesis after constriction initiation,
326 treadmilling promotes efficient constriction by increasing septal constriction rate. This reconciles
327 apparently contradictory models previously proposed for the role of FtsZ treadmilling in septal
328 constriction[1,3].

329

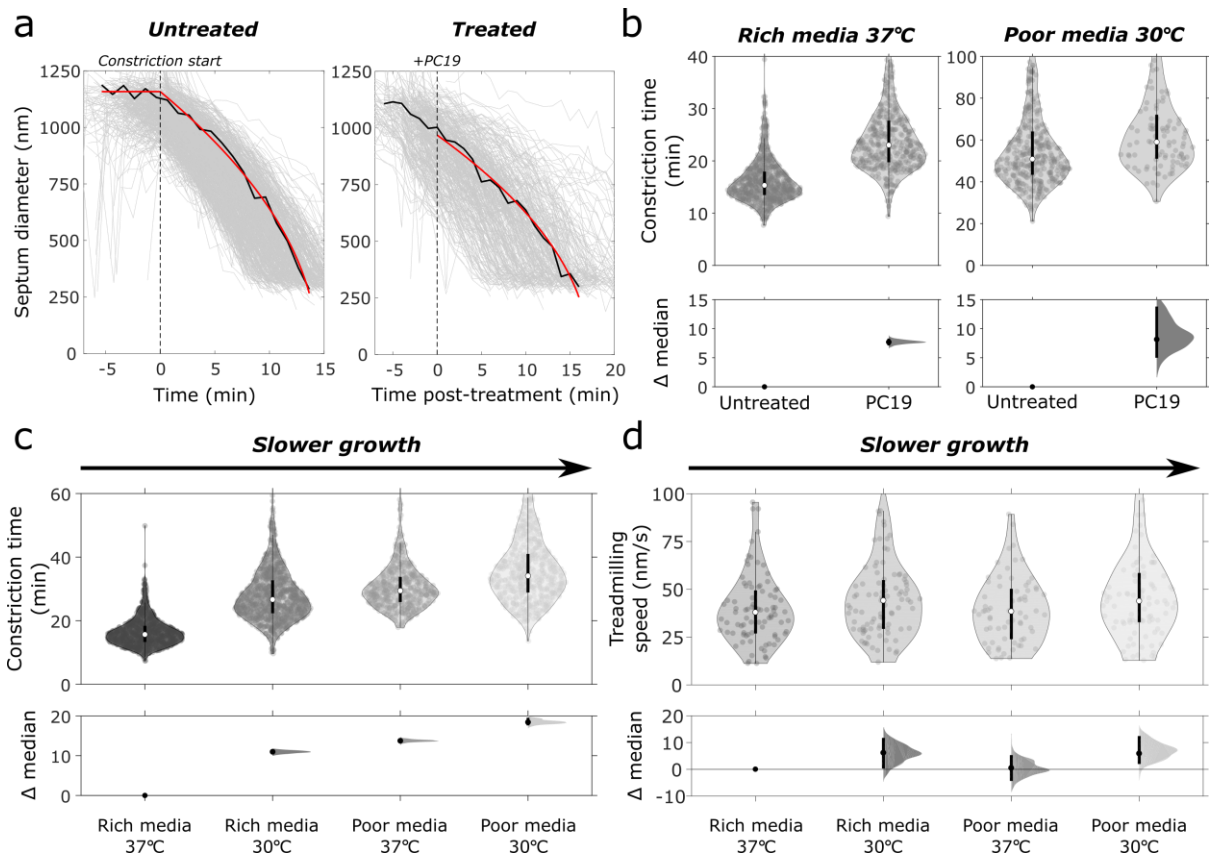

Figure 4. Constriction rate is accelerated by FtsZ treadmilling and fast cell growth rate. *(a) Time traces of ring diameters from mNeonGreen-PBP2B strain (ME7) for untreated (left) and PC19-treated (right) cells with constant PG synthesis model (red) fitted to representative traces (black).* Untreated cell trajectories are aligned relative to fitted constriction start time. PC19-treated cell trajectories are aligned relative to the arrival time of PC19-laced media. *(b) Constriction time before and after PC19 treatment for both fast growth (rich media 37°C) and slow growth (poor media, 30°C) conditions. (c) Constriction time of mNeonGreen-PBP2B cells in rich and poor media at two growth temperatures. (d) FtsZ-mNeonGreen (bWM4) treadmilling speeds in different media and temperature. Top panels, b-d:* violin plots; white circle, sample median; thick black lines, interquartile range; thin black lines, 1.5x interquartile range. *Bottom panels, b-d: Bottom panels:* DABEST plots showing effect size analysis, compared to leftmost condition; black circles, median difference; error bars, 95% confidence interval of median difference.

Cell growth rate limits septal constriction rate independently of FtsZ treadmilling

Growth rate and cell size for most bacterial species are linked to nutrient availability and culture temperature[33]. We sought to identify how growth rate affects the constriction rate of *B. subtilis* cells. We measured the constriction rate in media and temperature conditions (Supplementary Figure 3c; Supplementary Table 1) using a strain expressing PBP2B from its native promoter fused to mNeonGreen (ME7, Methods). We observed a linear dependence of septal constriction rate on overall cell growth rate (Supplementary Figure 3d). Slower growth in either minimal media or at low temperature led to correspondingly longer constriction times (Figure 4b, Supplementary Figure 3d), with a 2.18-fold (95% CI [2.12,2.24]) difference in constriction time between fastest and slowest growth conditions.

We considered that this difference in constriction time could result from a difference in the treadmilling speed of FtsZ across growth conditions. We therefore determined FtsZ treadmilling speed using TIRF illumination for all conditions using a dilute exogenous label of FtsZ-mNeonGreen (bWM4) which shows no growth or morphology phenotype at 37°C[1] (Supplementary Figure 23). FtsZ treadmilling speed was constant across all growth conditions tested (Figure 4d), showing that the effect of growth rate on septal constriction is independent of FtsZ treadmilling.

357 We next investigated whether FtsZ treadmilling also promotes constriction in slow growth conditions,
358 or if cell growth rate becomes the sole rate-limiting factor. As in fast growth conditions, arresting FtsZ
359 treadmilling increased the constriction time (Figure 4b, Supplementary Video 21). However, the
360 relative increase in constriction time was much lower in slow growth conditions (1.16-fold 95% CI
361 [1.09,1.24] vs 1.50-fold 95% CI [1.46,1.55] change). These observations show that cell growth rate is a
362 major regulator of active septal constriction, with treadmilling FtsZ filaments acting as a secondary
363 promotor of septal synthesis.

364 **DISCUSSION**

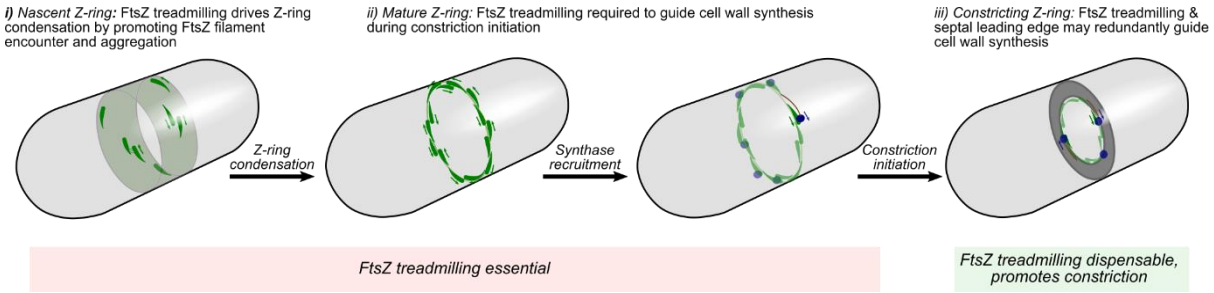

365
366 **Figure 5: Model for function of FtsZ treadmilling in Z-ring assembly and septal constriction.**

367 Using bespoke ultra-sensitive microscopy of cell division protein dynamics, we discovered that FtsZ
368 treadmilling plays two separate essential roles in cell division: to establish the mature divisome by
369 condensing diffuse filaments into a dense ring, and to guide septal constriction initiation (Figure 5).

370 We found that condensation of sparse FtsZ filaments into a stable, dense Z-ring structure is required
371 for cell division. Using VerCINI microscopy we observed that treadmilling FtsZ filaments frequently
372 collide and aggregate in nascent Z-rings. We also found that nascent Z-rings contain a large fraction of
373 immobile FtsZ filaments, which do not treadmill, and that Z-ring condensation promotes formation of
374 treadmilling FtsZ filaments. While the mechanism of FtsZ filament motility regulation requires further
375 study, *in vitro* measurements of FtsZ dynamics suggest that immobile FtsZ filaments could result from
376 low septal FtsZ concentration or regulation by accessory/anchor proteins[9].

377 Chemical arrest of FtsZ treadmilling completely abolished FtsZ ring condensation and septal
378 constriction. Attractive lateral interactions between FtsZ filaments, via the FtsZ C-terminal-linker and
379 cytoplasmic FtsZ-associated proteins are known to mediate FtsZ bundling and Z-ring condensation[34–
380 38]. Our results reveal an additional key factor in assembling the Z-ring: FtsZ filament treadmilling drives
381 filament interactions by enabling FtsZ filaments to rapidly search the mid-cell surface circumferentially
382 and efficiently encounter one another. We additionally found that rapid FtsZ filament turnover is
383 required for full condensation: slow turnover from reduced FtsZ GTPase activity led to partial filament
384 condensation into aberrantly-shaped Z-rings, and full inhibition of turnover from chemical arrest
385 prevented condensation entirely. These findings contrast with previous models of Z-ring condensation
386 involving lateral sliding of filaments[13,14]. We conclude that FtsZ treadmilling—likely along with FtsZ
387 lateral interactions—drives aggregation of FtsZ filaments into a condensed Z-ring. This is remarkably
388 reminiscent of treadmilling-driven partitioning of FtsZ filaments into higher-order structures
389 previously observed *in vitro*[9,39].

390 The second role of FtsZ treadmilling is to guide septal PG synthesis. We found that this role is essential
391 in the constriction initiation phase of *B. subtilis* cell division, but dispensable afterwards. Together with
392 our previous observations that FtsZ treadmilling guides individual synthase molecules during PG
393 synthesis[1], it is likely that during constriction initiation FtsZ filament treadmilling is required to guide
394 the synthases around the circumference of the mid-cell in the absence of an established septum. We

also observed that FtsZ treadmilling dynamics are division stage regulated, with Z-ring condensation promoting efficient FtsZ treadmilling. In addition to concentrating the division machinery into a small area, Z-ring condensation may indirectly promote efficient constriction initiation by increasing the fraction of treadmilling filaments available to guide cell-wall synthesis.

Although FtsZ treadmilling is dispensable after constriction initiation, we found that treadmilling increases the rate of septal constriction by up to 1.5-fold. However, we found that overall cell growth rate has a stronger effect on septal constriction rate than FtsZ treadmilling, increasing constriction rate up to 2.2-fold between fast and slow growth conditions. We conclude that FtsZ treadmilling plays a secondary role in active constriction, while its critical roles occur prior to constriction initiation. This contrasts with the previous model of *B. subtilis* FtsZ as an obligatory guide and rate-determining factor for constriction[1]. After constriction initiation, the highly ordered septal leading edge[40] may be sufficient to act as a guide for processive septal PG synthesis, with FtsZ filaments acting as a mid-cell localiser and redundant guide during active constriction.

Surprisingly, we found that the *B. subtilis* septal constriction and overall cell growth rate are strongly coupled, with a linear dependence of septal constriction rate on cell growth rate. The molecular mechanism of coupling between septal constriction and cell growth rate requires further research, but possibilities include control of septal synthesis via overall levels of cell wall precursor[41,42] or levels of cell wall synthesis proteins, or direct regulation of cell wall synthesis protein activity via signalling[43].

The VerCINI method presented here is a powerful tool for ultra-sensitive measurement of cell division protein dynamics and mode of action of cell division targeting antibiotics. We anticipate that many other bacterial structures, especially the bacterial cell envelope and associated proteins, could also benefit from VerCINI's high resolution top-down cell view.

A key puzzle in bacterial cell biology is how nanoscale division proteins spontaneously and accurately build a micron-size wall at mid-cell. Treadmilling gives FtsZ filaments the remarkable ability to autonomously drive their own circumferential motion around the mid-cell surface. Our results show that the self-driving capability of FtsZ filaments is crucial to solving the scale problem of cell division by directing divisome assembly and initial septal synthesis to a narrow band around the mid-cell, laying the template for septum construction. Dynamic, self-organizing FtsZ filaments thus provide long-distance order and collective motion around the bacterial mid-cell in the absence of cytoskeletal motor proteins.

ACKNOWLEDGEMENTS

We thank Henrik Strahl (Newcastle) for helpful discussions, Ling Wu and Jeff Errington (Newcastle) for strains and antibodies, Luke Lavis (HHMI) for Janelia Fluor dyes, and Ethan Garner (Harvard) for strains. SH, KW, CJ and EK acknowledge funding support by a Newcastle University Research Fellowship and a Wellcome Trust & Royal Society Sir Henry Dale Fellowship grant number 206670/Z/17/Z. NT supported by a UK Engineering and Physical Sciences Research Council doctoral studentship. RH and PA funded by grants from the UK Biotechnology and Biological Sciences Research Council (BB/M022374/1), the UK Medical Research Council (MR/K015826/1), and Wellcome Trust (203276/Z/16/Z). CD and KW acknowledge funding support by ERC grant SynDiv (669598) and the Netherlands Organisation for Scientific Research (NWO/OCW) as part of the Frontiers of Nanoscience and Basyc programs.

AUTHOR CONTRIBUTIONS

KW, CJ and NT acquired data. KW, CJ, NT and SH analysed data. KW, CJ, SH and CD developed the VerCINI method. KW performed nanofabrication, supervised by CD. SH, KW, PA and RH wrote

438 software. CJ, EK, NT, and KW created and characterised bacterial strains. SH and CD directed the
439 research. KW, SH and CJ wrote the manuscript with input from all authors.

440 **Materials and Methods**

441 **Bacterial strains and growth conditions**

442 Strains used in this study are listed in Supplementary Table 2. Strains were streaked from -80°C freezer
443 glycerol stocks onto Nutrient Agar (NA) plates containing the relevant antibiotics and/or inducers and
444 grown overnight at 37°C. Single colonies were transferred to liquid starter cultures in either Time-
445 Lapse Medium (TLM[45]) or PHMM media and grown with agitation at 200 rpm overnight at either 30°C
446 (TLM) or 22°C (PHMM[1]). The next day, TLM starter cultures were diluted to a starting OD_{600} of 0.1 in
447 Chemically-Defined Medium (CDM[45]), while PHMM starter cultures were diluted to a starting OD_{600} of
448 0.05 in PHMM, and these liquid cultures were grown at 30°C or 37°C with any required inducer until
449 they reached the appropriate OD_{600}. When necessary, antibiotics and inducers were used at the
450 following final concentrations: chloramphenicol 5 µg/ml, spectinomycin 60 µg/ml, erythromycin
451 1 µg/ml, lincomycin 10 µg/ml, kanamycin 5 µg/ml, xylose 0.08% and IPTG 20 µM.

452 **Strain construction**

453 **SH211** (PY79 Δ*hag*) was constructed by transforming competent PY79 with genomic DNA extracted
454 from strain PB5250, using standard protocols[46]. The antibiotic resistance cassette was removed using
455 pDR224 as described previously[47].

456 **SH130** (PY79 Δ*hag ftsZ::ftsZ-gfp-cam*) was constructed by transforming SH211 competent cells with
457 genomic DNA extracted from strain PL642.

458 **SH131** (PY79 Δ*hag ftsZ::ftsZ-gfp-cam* Ω *amyE::erm*-$P_{hyperspank}$-*ftsAZ*(D213A)) was constructed by
459 transforming competent SH130 cells with genomic DNA extracted from strain bAB215.

460 **SH132** (PY79 *pbp2B::mNeonGreen-15aa-pbp2B* Ω *amyE::erm*-Phyperspank-*ftsAZ*(D213A)) was
461 constructed by transforming competent ME7 cells with genomic DNA extracted from strain bAB215.

462 **SH212** (PY79 *pbp2B::erm*-$P_{hyperspank}$-*HaloTag-15aa-pbp2B* Ω *amyE::spc* P_{xyl} *gfp-ftsZ*) was constructed by
463 transforming competent bGS28 cells with genomic DNA extracted from strain 2020. All published
464 strains are available on request to the authors.

465 **Bacterial strain characterization**

466 Strains were characterised by growth in liquid culture (Supplementary Figure 3) and cell morphology
467 analysis (Supplementary Figure 2). Fluorescent fusion protein levels for relevant strains were
468 determined by Western blotting (Supplementary Figure 1).

469 **Growth curves**

470 *B. subtilis* PY79 and variant strains were grown overnight in TLM or PHMM containing the relevant
471 inducers. Overnight cells were diluted to an OD_{600} of 0.05 in either CDM or PHMM, respectively, and
472 200 µL were used in a 96-well microtiter plate. Growth was monitored for 12 hours using a FluoStar
473 plate reader (BMG Labtech).

474 **Cell morphology analysis**

475 PY79 and SH130 cultures were prepared for imaging in CDM or PHMM as described above. Once the
476 cultures had reached OD_{600} 0.4-0.5, Nile Red was added to 200 µl of cells to a working concentration
477 of 1 µg/ml, and incubated at growth temperatures for 5 mins, prepared on agarose microscope slides

478 as described below and cell morphology images recorded. Cell length was then manually determined
479 using ImageJ.

480 **Western blotting**

481 Overnight cultures of specified strains were grown overnight in LB at 30°C. The following morning,
482 cultures were diluted to ~OD_{600} 0.05 and grown at 30°C until ~OD_{600} 0.6. Cells were harvested by
483 centrifugation and stored at 20°C for further processing. Samples were normalised based on OD600,
484 re-suspended in 2x SDS protein sample buffer and heated at 80°C for 10 minutes followed by
485 centrifugation.20 µL lysates were then separated by SDS PAGE in 10% polyacrylamide gel.. FtsZ and
486 PBP2B were detected using a FtsZ polyclonal (Sigma, 1:10000 dilution) and a PBP2B polyclonal (Merck,
487 1:5000 dilution) antibody, respectively, followed by a HRP-conjugated anti-rabbit IgG antibody
488 (Sigma). Samples were developed using Pierce™ ECL Western Blotting Substrate (Thermofisher) and
489 imaged using an ImageQuant LAS 4000 mini Biomolecular Imager (GE Healthcare).

490 **Microscopy**

491 Power density, exposure time and other key parameters are listed for each microscopy experiment in
492 Supplementary Table 4. All imaging was done using either a Nikon N-SIM/N-STORM inverted
493 fluorescence microscope (Figure 4, Supplementary Figure 23) or a custom-built inverted microscope
494 (otherwise).

495 *Nikon N-STORM.* Cells were illuminated with a 488 nm line from an Argon Ion laser (CVI Melles-Griot).
496 A 100x TIRF objective (Nikon CFI Apochromat TIRF 100XC Oil) was used for imaging and an Andor iXon
497 DU897 EMCCD camera was used, with a 1.5x OptoVar (Nikon) and standard Nikon tube lens, giving an
498 effective image pixel size of 106 nm/pixel. Cells were illuminated via HiLO[48] inclined illumination to
499 minimise background using an objective TIRF module (Nikon N-STORM module) using 488 nm laser
500 excitation.

501 *Custom microscope.* Cells were illuminated with a 488 nm laser (Obis) and/or a 561 nm laser (Obis) as
502 indicated. A 100x TIRF objective (Nikon CFI Apochromat TIRF 100XC Oil) was used for all experiments
503 except microfluidic VerCINI measurements where a 100x silicone immersion objective (CFI SR HP Plan
504 Apochromat Lambda S 100XC Sil, Nikon) was used for deep focusing. A 200 mm tube lens (Thorlabs
505 TTL200) and Prime BSI sCMOS camera (Teledyne Photometrics) were used for imaging, giving effective
506 image pixel size of 65 nm/pixel. Imaging was done with a custom-built ring-TIRF module operated in
507 ring-HiLO[48] using a pair of galvanometer mirrors (Thorlabs) spinning at 200 Hz to provide uniform, high
508 SNR illumination.

509 **Nanofabrication**

510 Micropillars were patterned using electron-beam lithography and etched using reactive-ion etching.
511 Briefly, a silicon wafer was spin coated with AR-N 7700.18 (Allresist GmbH). Features were patterned
512 using a Leica EBPG 5000+ with 56 nm beam step size. The unexposed resist was removed with solvent
513 Microposit MF-321 and the exposed wafer surface was etched using an AMS Bosch etcher. The
514 remaining resist was removed using oxygen plasma. Pillars widths ranged from 1.0 to 13 µm with
515 height 6.7 µm, spaced 5 µm apart. Final micropillar dimensions were confirmed using SEM.

516 Micropillar wafers were silanised to allow cured polydimethylsiloxane (PDMS) to be removed without
517 damaging structures. To do this, wafers were coated with (tridecafluoro-1,1,2,2-tetrahydrooctyl)
518 trichlorosilane (abcr GmbH) by vapour deposition.

519 **VerCINI**

520 Agarose microholes were formed by pouring molten 6% agarose onto the silicon micropillar array.
521 Patterned agarose was transferred into a Geneframe (Thermo Scientific) mounted on a glass slide, and
522 excess agarose was cut away to ensure sufficient oxygen. Cells at $OD_{600} \sim 0.4$ were concentrated 100x
523 by centrifugation and added onto the agarose pad. Cells were then loaded into the microholes by
524 centrifuging the mounted agarose pad with concentrated cell culture in an Eppendorf 5810 centrifuge
525 with MTP/Flex buckets. Unloaded cells were rinsed off with excess media.

526 FtsZ treadmilling dynamics were imaged at 1 frame/s (continuous exposure) for 2 mins at 1-8 W/cm^2.
527 After each field of view was imaged, a multi-slice Z-stack was taken at 500 nm intervals to exclude
528 tilted or improperly trapped cells, in addition to excluding Z-rings that have an adjacent Z-ring 1 µm
529 above or below the imaging plane. VerCINI experiments were performed on cells in a *Δhag* mutant
530 background, preventing undesirable cell rotation within the microholes by disabling flagellar motility.

531 **Microfluidic VerCINI**

532 *Device assembly*

533 Open-topped microhole coverslips were formed from PDMS using the silicon micropillar array
534 (Supplementary Figure 24). All PDMS reagents and processing equipment were from BlackHoleLab.
535 PDMS elastomer base and curing agent were mixed in a 1:1 ratio and degassed. The degassed mixture
536 was then poured on top of the microhole array and a microscope coverslip was pressed down to form
537 a thin layer. PDMS was cured by baking at 80°C for 1 hr, and the coverslip with patterned PDMS layer
538 was removed from the silicon mould.

539 Microfluidic chambers were prepared using readily-available components (Supplementary Figure 24).
540 First, holes were drilled into a glass microscope cover slide using a diamond drill bit (Kingsley North).
541 A flow channel was then made by cutting a strip of double-sided tape using either a scalpel or laser
542 engraver. One side of the double-sided tape was then adhered to the microscope cover slide. Cut
543 pipette tips were then inserted into the drilled holes, and polyethylene tubing (Smiths Medical) was
544 inserted into them. Leakage was prevented by sealing pipette tips and tubing using epoxy.

545 To load cells into the microholes, PDMS was first rendered hydrophilic by treating with air plasma for
546 3 min. A 9 mm diameter silicone gasket (Grace Bio-Labs) was then placed over the PDMS microholes.
547 Cells at $OD_{600} \sim 0.4$ were concentrated 100x by centrifugation and pipetted into the silicone gasket.
548 Cells were then loaded into the microholes by centrifuging the microhole-containing coverslip with
549 concentrated cell culture in an Eppendorf 5810 centrifuge with MTP/Flex buckets. The coverslip was
550 covered during centrifugation to prevent evaporation. Unloaded cells were rinsed off with excess
551 media. To ensure adequate loading, this loading-and-rinsing protocol was then repeated.

552 After cells were loaded into microholes, the silicone gasket was removed and the flow chamber was
553 fully assembled by adhering the PDMS-covered coverslip to the exposed side of double-sided tape on
554 the glass cover slide (Supplementary Figure 24).

555 *Imaging*

556 Due to the relatively thick (~50 µm) layer of PDMS between the coverslip surface and the confined
557 cells, a Nikon silicone immersion objective (CFI SR HP Plan Apochromat Lambda S 100XC Sil, Nikon)
558 was used for imaging due to its high working distance (0.3 mm).

559 Since the indices of refraction for PDMS and aqueous solution are similar, autofocusing systems relying
560 on the reflection of an IR signal from two interfaces were not adequate due to weak signal. Instead,
561 autofocusing was done using an image-based approach first described by McGorty and co-workers[25]
562 using cross-correlation of brightfield images. Briefly, a separate brightfield imaging pathway was

563 added to the microscope using a 1050 nm IR LED (Thorlabs) and IR-sensitive camera (UI-1220LE-M-GL,
564 Imaging Development Systems GmbH), and a plugin for Micro-Manager was developed to calculate
565 cross-correlations and move the sample stage (https://github.com/HoldenLab/DeepAutoFocus). At
566 the start of an experiment, a z-stack of IR brightfield images was obtained as a reference. During the
567 experiment, the cross-correlation map between every new IR brightfield image and this reference
568 stack was calculated, and the sample stage was moved to compensate for any drift. To our knowledge
569 this is the first application of IR cross-correlation autofocusing to live cell imaging.

570 *Fluid control*

571 Media was flowed through the chamber by a syringe pump (Aladdin-220, World Precision
572 Instruments). To prevent potential leakage, media was pulled through the chamber from fluid
573 reservoirs by operating the syringe pump in withdraw mode. Complete solution exchange occurred
574 within 7 s of initial compound arrival time, estimated using a rhodamine tracer.

575 **CellASIC experiments**

576 The microfluidic CellASIC system (EMD Millipore) was used to image constricting cells during
577 treatment with division inhibitors. Cells were loaded into B04A plates and equilibrated in blank media
578 for ~15 min with a pressure of 2 psi (~6 µL/hr flow rate) prior to imaging.

579 In a typical experiment, untreated constricting cells were imaged for 30 min (1 min/frame, 1 s
580 exposure, 1-2 W/cm^2) while blank media was flowed using 2 psi. Solution exchange was done by first
581 flowing media with compound using 8 psi (~34 µL/hr flow rate) for 15 s, then dropping the pressure
582 to 2 psi for the remainder of the experiment (50-90 min). DMSO treatment alone caused a small but
583 robust increase in constriction time (Supplementary Figure 25). However, pre-adaptation of cells to
584 blank media containing DMSO eliminated this effect, showing that observed effects of PC19 treatment
585 resulted from the drug and not the solvent that accompanied it (Supplementary Figure 25).

586 The arrival time of the compound at the cells was most estimated by treating the FtsZ-GFP strain with
587 10 µM PC19 using our standard flow protocol. PC19 causes the diffuse cytoplasmic FtsZ-GFP to rapidly
588 polymerise into short filaments throughout the cell (Supplementary Videos 10-13), providing a clear
589 signal for compound arrival. From these experiments we determined that compound arrives 3-4 min
590 after fluid exchange.

591 **Microscopy of horizontal cells**

592 *Sample preparation*

593 Coverslips were first cleaned by treating with air plasma for 5 min. Slides were prepared as described
594 previously[45]: Flat 2% agarose pads of either CDM or PHMM were prepared inside Geneframes (Thermo
595 Scientific) and cut down to strips of 5 mm width to ensure sufficient oxygen supply to cells. Cell
596 cultures were grown to OD_{600} between 0.2 and 0.4, when 0.5 µL of cell culture was spotted on the
597 pad. Cells were allowed to adsorb to the pad for 30 s before a plasma-cleaned coverslip was placed
598 on them. After spotting on agarose pads, cells were allowed to equilibrate within the microscope body
599 for 15 min before being imaged. Cells were then imaged either by TIRF microscopy for observation of
600 FtsZ filament dynamics, or ring-HiLO for time-lapse observation, with experimental parameters
601 defined in Supplementary Table 4.

602 *HaloTag labelling with JF549 dye*

603 Full labelling of HaloTag-PBP2B was done by incubating strain SH212 with 50 nM JF549 HaloTag ligand
604 for 15 min. Cells were washed once with fresh media before imaging. JF549 HaloTag ligand was a gift
605 from Luke Lavis[32].

606 **Image analysis**

607 ***VerCINI data analysis***

608 *Pre-processing*

609 Videos were denoised using the ImageJ plugin PureDenoise[17], which is based on wavelet
610 decomposition. Key assumptions of the method are (i) local spatiotemporal similarity within the
611 image (ii) absence of sharp discontinuities, guaranteed by diffraction-limited nature of the image. The
612 denoising algorithm makes does not make any assumptions on the type of underlying biological
613 structure.

614 Denoised videos were registered using the ImageJ plugin StackReg[49]. Image stacks of vertically
615 immobilised cells were inspected to exclude tilted cells or out of focus FtsZ-rings, or FtsZ rings where
616 a second Z-ring was closer than 1 um to the focal plane. Cropped region of interest movies containing
617 single in-focus cells were manually selected and exported for analysis. An ImageJ package for VerCINI
618 data processing is available (https://github.com/HoldenLab/Ring_Analysis_IJ).

619 *VerCINI background subtraction, kymograph extraction, quantification*

620 Custom software for quantitative cytoplasmic background subtraction and kymograph extraction was
621 developed for analysis of VerCINI movies (https://github.com/HoldenLab/ring-fitting2). Fluorescence
622 images of isolated vertical cells were fitted to a joint explicit model for diffuse out-of-focus cytoplasmic
623 background (Gaussian + Cauchy model) plus septal protein signal, modelled as a 12 sectored annulus
624 with each sector of variable amplitude.

625 $$F(x,y) = Signal(x,y) + Bg(x,y)$$

626 Signal is calculated in polar coordinates, around the septal ring centre fit parameter (x_0, y_0), and then
627 transformed into Cartesian coordinates. Signal is defined as

628 $$S(r,\theta) = A_i(\theta)\exp\left(-\frac{(r-R_0)^2}{2\sigma^2}\right),$$

629 where $A_i(\theta)$ defines a 12 sectored ring. Background is defined as

630 $$Bg(x,y) = a\exp\left(\frac{-((x-x_0)^2+(y-y_0)^2)}{2\sigma_{bg1}^2}\right) + b\frac{\sigma_{bg2}^2}{(x-x_0)^2+(y-y_0)^2+\sigma_{bg2}^2} + c.$$

631 This explicit model allowed accurate sub-pixel location of a circular line profile at the septal leading
632 edge. Explicit subtraction of complex background signal also allowed septal intensity quantification.
633 The background subtracted intensity along the circular line profile was then calculated for each frame
634 and automatically plotted as a kymograph. Kymographs were plotted over the [0,720°] ie two
635 complete revolutions around the line profile for ease of visualization, specifically to allow
636 straightforward visualization of treadmilling filaments crossing the 360°,0° boundary. For each cell,
637 the Z-ring diameter was determined from the fitted model in the kymograph extraction step. Median
638 septal intensity was calculated as the median value of all kymograph pixels from the first 60 image
639 frames.

640 *FtsZ filament treadmilling analysis using VerCINI*

641 We found that automated methods for in vitro FtsZ filament speed measurements, either after Dos
642 Santos Caldas and coworkers[50] or using a similar in-house algorithm, are currently insufficient for FtsZ
643 filament speed analysis in either horizontal or vertical cells compared to manual analysis, because at
644 cellular filament density they currently perform poorly at detecting immobile filaments, break the

645 complete trajectories of treadmilling filaments into multiple shorter trajectories, and cannot reliably
646 process images from dense Z-rings in horizontal cells.

647 We therefore performed manual measurement of filament speed and processivity by kymograph
648 analysis, annotating filaments as lines in ImageJ and then measuring the angle via ImageJ script. As
649 the intensity range across kymographs is large, manual detection and analysis of filaments was aided
650 by applying a ridge filter[51] to the kymograph which detects ridges in the image, independent of
651 absolute intensity. The ridge filter consists of a Gaussian blur operation to set the feature scale and
652 suppress noise (here 2 pixels, 130 nm), followed by calculation of the major eigenvalue of the Hessian
653 matrix for each pixel, implemented as an ImageJ macro in the package listed above. Joint annotation
654 of the ridge filtered and raw intensity kymograph was performed, allowing sensitive annotation of
655 both bright and dim filaments (Supplementary Figure 26).

656 ***Horizontal cell image analysis***

657 *Pre-processing*

658 Images were denoised and registered as described above.

659 *Cell segmentation and tracking of division protein localization*

660 MicrobeJ[11] was used to track individual FtsZ-/PBP2B-rings and export their centroid coordinates for
661 analysis. To do this, image backgrounds were first subtracted using a sliding paraboloid window of 50
662 pixels and all frames were converted to 8-bit for easier thresholding.

663 Two approaches were used to identify division protein localization, depending on the experiment. For
664 measurements of septal constriction rate only (Figure 4a), which requires only detection of bright
665 dense FtsZ/PBP2B rings, a simple approach of intensity-based threshold detection was applied in
666 MicrobeJ a threshold was selected manually for each field of view using MinError. Additional area and
667 length thresholds (Area: [0.08 Inf] μm^2, Length: [0.02 1.8] µm) were established to exclude objects in
668 fields of view that were not rings. Tracks shorter than 7 frames were excluded. Data was then exported
669 for analysis in MATLAB.

670 For analysis of FtsZ ring dynamics over the entire division process, from nascent Z-ring assembly to
671 late constriction (Figure 1), it was necessary to additionally robustly detecting diffuse patchy FtsZ-
672 rings. We trained the machine learning segmentation tool Ilastik[12] to detect cell outlines with
673 fluorescence images of cells labelled with FtsZ. For detection of diffuse Z-rings, we applied a large
674 Gaussian blur filter to the images, and then multiplied this by the Ilastik-segmented binary image,
675 which had the effect of separating any overlap of Z-rings between adjacent cells. Intensity threshold-
676 based detection of Z-rings was then performed in MicrobeJ as above.

677 *Quantification of division protein septal localization*

678 Custom MATLAB software was developed to measure the diameters and intensities of Z- and 2B-rings
679 obtained from either MicrobeJ or Ilastik. Each frame of each individual ring was first segmented using
680 a multi-level threshold to distinguish the septum, cytoplasm, and background. The septal axis and the
681 cell axis were identified using the segmented image, and the image was rotated such that pixels were
682 aligned along these axes. Line profiles of Z- and 2B-rings were obtained by averaging pixel values along
683 the septal axis ±2 pixels to reduce noise. Diameter were then obtained by fitting line profiles to a toy
684 model that describes a circle of uniform intensity rotated to be orthogonal to the axis of the imaging
685 plane ('Tilted Circle Model', Supplementary Note 1, Supplementary Figure 27). Septal density was
686 calculated as the total intensity along the lateral line profile, divided by the ring circumference, as
687 calculated from the constriction rated analysis (below) to reduce single frame noise. Septal density

688 was used in place of total intensity, in order to compare to the septal intensity measurements
689 obtained during the VerCINI experiments. Axial thickness was estimated by fitting an axial line profile
690 to an analytical super-Gaussian and calculating the full-width half maximum.

691 *Evaluation of percentage Z-rings condensed and constricted post-treatment*

692 Since PC19 treatment causes bright fluorescent foci to appear randomly throughout the cell in strains
693 where FtsZ is labelled, tracking software fails to consistently follow most Z-rings post-treatment in the
694 SH130 and SH212 strains. Furthermore, measurements of Z-ring thickness and diameter were
695 inaccurate due to the proximity of fluorescent foci. Since it was typically straightforward to observe,
696 whether Z-rings condensed and/or constricted post-PC19 treatment was evaluated manually.

697 *FtsZ filament treadmilling analysis from TIRF microscopy data*

698 Images were denoised and registered as above. TrackMate[52] was used to help identifying treadmilling
699 FtsZ filaments outside of dense Z-rings. A line region of interest (ROI) was drawn perpendicular to the
700 cell axis where treadmilling filaments were identified. Kymographs were calculated along this line
701 profile FtsZ filaments trajectories in the kymograph were marked with a line ROI (Supplementary
702 Figure 23). Treadmilling speed for each filament trajectory was calculated from the angle of the line
703 ROIs.

704 ***Constriction rate analysis***

705 Previous models for septal constriction have either been *ad hoc*[26] or tailored to Gram-negative cell
706 division based on remodelling of a hemispherical cap[27]. We derived a simple model for Gram-positive
707 constriction, assuming (i) outside-in synthesis of a flat plate at mid-cell and (ii) total PG synthesis rate
708 around the septal leading edge is constant (Supplementary note 2)

709
$$d(t) = \begin{cases} d_0, & t < t_0 \\ \sqrt{d_0^2 - \frac{4k}{\pi}(t - t_0)}, & t \geq t_0 \end{cases}$$

710 Where d_0 is the initial Z- or 2B-ring diameter, t_0 is the time constriction begins, and k is the rate at
711 which area is added to the septal plate. This model fitted measured constriction trajectories well, and
712 the estimated time of constriction completion corresponded closely to completion times
713 independently estimated from PBP2B departure in wild type cells (Supplementary Figure 28).

714 We measured constriction rates in the mNeonGreen-PBP2B strain, since FtsZ-GFP mislocalises post-
715 treatment with PC19 and makes it difficult to track large numbers of septa. A small amount of
716 mNeonGreen-PBP2B signal remained at mid-cell after constriction had finished. This excess signal was
717 excluded from the rate analysis by cutting the 2B-ring data after this drop in intensity. We obtained
718 constriction time distributions for PC19-treated cells by fitting only to post-treatment data.

719 For comparison to previous observations we converted the observed constriction rates to an effective
720 constriction time t_{eff}, the total amount of time it would take for an unconstricted septum to constrict
721 completely (Methods) given the fitted rate k : $t_{eff} = 2\pi \cdot \frac{d_0^2}{k}$. The average diameter of the
722 unconstricted septum d_0 was estimated as 1100 ± 100 nm (mean, SD) for the mNeonGreen-PBP2B
723 based on the background fluorescence signal in the cell.

724 **Statistics**

725 Data were analysed using estimation statistics, which focusses on magnitude and robustness of effect
726 size using DABEST[53] (Data Analysis with Bootstrap Coupled Estimation), rather than just statistical
727 significance/ p-value. Averages reported were median values unless otherwise indicated.

728 The basic principle of a DABEST plot is to calculate and plot the average (here median) difference
729 between two conditions, together with the 95% confidence interval on that difference. This has the
730 advantage over null hypothesis significance testing (NHST) of visualising not just the probable
731 reproducibility of a difference between two conditions, but also the estimated magnitude of the
732 difference between the two conditions. This is useful because it allows assessment of whether
733 magnitude of difference is physically/ biologically meaningful, rather than just reproducible. For
734 comparison to NHST analysis, we note that a median difference DABEST plot where the 95 % CIs do
735 not overlap the 0-difference axis would indicate rejection of the null hypothesis that the two
736 population medians are equal at p=0.05 significance level.

737 All effect size estimates were calculated based on difference of medians. 95% confidence interval of
738 the median, or of the difference of medians, was estimated by bootstrapping
739 (https://github.com/HoldenLab/violinplusDABEST-Matlab) and indicated with square brackets [].
740 Interquartile range was indicated by IQR. Thick error bar lines in Violin plots indicate interquartile
741 range, thin lines indicate adjacent vales. Error bars in DABEST plots indicate 95% CI of median
742 difference, estimated by bootstrapping. Sample size, indicating number of filaments/Z-ring, cells,
743 microscope fields of view, technical and biological replicates, as appropriate, is presented for each
744 dataset in Supplementary Table 3.

745 **Simulations of FtsZ filament dynamics**

746 Simulated time lapse movies of FtsZ filament dynamics in vertically immobilized cells were generated.
747 Source code for simulations is available (https://github.com/HoldenLab/ring-simulator). Filament
748 speed and lifetime were sampled from distributions obtained from experiments via bootstrap
749 resampling. FtsZ filament distributions were taken from cells expressing FtsZ-GFP in the nascent Z-ring
750 cell division state. Sub-diffraction-limited treadmilling filaments were simulated on a diffuse Gaussian-
751 Cauchy cytoplasmic background described above. Filament intensity, background amplitude and
752 shape parameters all matched average parameters experimentally measured in the VerCINI images of
753 nascent Z-rings. Photon noise and manufacturer specified camera gain and read noise were added to
754 the images.

755 The number of filaments in each simulated Z-ring was drawn from a Poisson distribution with average
756 filament density equal to observed nascent, mature, 2x mature or 12x mature Z-ring density of (1.3,
757 3.3, 6.5, 37.5 filaments/ Z-ring/ frame). Filament density of real nascent Z-rings was calculated directly
758 from observed number of manually traced filaments. Filament density in mature Z-rings was
759 estimated by multiplying the estimated nascent Z-ring density by 2.6, the ratio of total Z-ring intensity
760 for mature and nascent Z-rings (Supplementary Figure 8b).

761 **Step finding analysis of Z-ring axial thickness data**

762 Transitions between a decondensed and condensed Z-ring for SH130 cells expressing FtsZ-GFP Z-rings
763 was measured using a step finding algorithm to detect either one or two states in time series Z-ring
764 axial thickness, using a global change point detection algorithm[54] implemented in the MATLAB
765 function *findchangepts().* State detection was performed based on changes in standard deviation of
766 the time series, with an additional threshold that detected axial thickness states should differ by at
767 least 50 nm.

768 **Analysis of Z-ring axial thickness data for FtsZ(D213A) mutant**

Although the step-finding method described above accurately located the decondensed-to-condensed transition in wild-type cells, we found that this method was inadequate for the FtsZ(D213A) mutant since these Z-rings were in a partially-condensed state and did not show a similar transition as wild-type. Instead, we considered these Z-rings as "low thickness pre-constriction" if their thicknesses dropped below a threshold value for at least one frame (1 min) prior to the start of constriction. The threshold was chosen as 1σ above the mean thickness for condensed wild-type cells (356 nm; Supplementary Figure 17).

DATA AVAILABILITY

Source data for all figures presented in the paper and Supplementary Information, as well as raw movie files for all Supplementary Videos are available at

https://data.ncl.ac.uk/projects/FtsZ_treadmilling_is_essential_for_Z-ring_condensation_and_septal_constriction_initiation_in_Bacillus_subtilis_cell_division/92465

CODE AVAILABILITY

Custom software is available on the Holden lab GitHub page:

https://github.com/HoldenLab/Ring_Analysis_IJ
https://github.com/HoldenLab/ring-fitting2
https://github.com/HoldenLab/DeepAutoFocus
https://github.com/HoldenLab/ring-simulator

788 **REFERENCES**

789 1. Bisson-Filho, A. W. *et al.* Treadmilling by FtsZ filaments drives peptidoglycan synthesis and
790 bacterial cell division. *Science* **355**, 739–743 (2017).
791 2. Yang, X. *et al.* GTPase activity–coupled treadmilling of the bacterial tubulin FtsZ organizes septal
792 cell wall synthesis. *Science* **355**, 744–747 (2017).
793 3. Monteiro, J. M. *et al.* Peptidoglycan synthesis drives an FtsZ-treadmilling-independent step of
794 cytokinesis. *Nature* (2018) doi:10.1038/nature25506.
795 4. Perez, A. J. *et al.* Movement dynamics of divisome proteins and PBP2x:FtsW in cells of
796 Streptococcus pneumoniae. *Proc. Natl. Acad. Sci.* **116**, 3211–3220 (2019).
797 5. Baranova, N. *et al.* Diffusion and capture permits dynamic coupling between treadmilling FtsZ
798 filaments and cell division proteins. *Nat. Microbiol.* **5**, 407–417 (2020).
799 6. Yao, Q. *et al.* Short FtsZ filaments can drive asymmetric cell envelope constriction at the onset of
800 bacterial cytokinesis. *EMBO J.* e201696235 (2017) doi:10.15252/embj.201696235.
801 7. Strauss, M. P. *et al.* 3D-SIM Super Resolution Microscopy Reveals a Bead-Like Arrangement for
802 FtsZ and the Division Machinery: Implications for Triggering Cytokinesis. *PLoS Biol* **10**, e1001389
803 (2012).
804 8. Holden, S. J. *et al.* High throughput 3D super-resolution microscopy reveals *Caulobacter*
805 *crescentus* in vivo Z-ring organization. *Proc. Natl. Acad. Sci.* **111**, 4566–4571 (2014).
806 9. Loose, M. & Mitchison, T. J. The bacterial cell division proteins FtsA and FtsZ self-organize into
807 dynamic cytoskeletal patterns. *Nat. Cell Biol.* **16**, 38–46 (2014).
808 10. Levin, P. A., Kurtser, I. G. & Grossman, A. D. Identification and characterization of a negative
809 regulator of FtsZ ring formation in Bacillus subtilis. *Proc. Natl. Acad. Sci.* **96**, 9642–9647 (1999).
810 11. Ducret, A., Quardokus, E. M. & Brun, Y. V. MicrobeJ, a tool for high throughput bacterial cell
811 detection and quantitative analysis. *Nat. Microbiol.* **1**, 1–7 (2016).
812 12. Berg, S. *et al.* ilastik: interactive machine learning for (bio)image analysis. *Nat. Methods* **16**, 1226–
813 1232 (2019).

814 13. Monahan, L. G., Robinson, A. & Harry, E. J. Lateral FtsZ association and the assembly of the
815 cytokinetic Z ring in bacteria. *Mol. Microbiol.* **74**, 1004–1017 (2009).
816 14. Erickson, H. P., Anderson, D. E. & Osawa, M. FtsZ in Bacterial Cytokinesis: Cytoskeleton and Force
817 Generator All in One. *Microbiol. Mol. Biol. Rev.* **74**, 504–528 (2010).
818 15. Walker, B. E., Männik, J. & Männik, J. Transient Membrane-Linked FtsZ Assemblies Precede Z-Ring
819 Formation in Escherichia coli. *Curr. Biol.* **30**, 499–508.e6 (2020).
820 16. Ellefsen, K. L., Dynes, J. L. & Parker, I. Spinning-Spot Shadowless TIRF Microscopy. *PLOS ONE* **10**,
821 e0136055 (2015).
822 17. Luisier, F., Vonesch, C., Blu, T. & Unser, M. Fast interscale wavelet denoising of Poisson-corrupted
823 images. *Signal Process.* **90**, 415–427 (2010).
824 18. Haydon, D. J. *et al.* An Inhibitor of FtsZ with Potent and Selective Anti-Staphylococcal Activity.
825 *Science* **321**, 1673–1675 (2008).
826 19. Elsen, N. L. *et al.* Mechanism of action of the cell-division inhibitor PC190723: Modulation of FtsZ
827 assembly cooperativity. *J. Am. Chem. Soc.* **134**, 12342–12345 (2012).
828 20. Wagstaff, J. M. *et al.* A polymerization-associated structural switch in FtsZ that enables
829 treadmilling of model filaments. *mBio* **8**, e00254-17 (2017).
830 21. Artola, M. *et al.* The structural assembly switch of cell division protein FtsZ probed with
831 fluorescent allosteric inhibitors. *Chem. Sci.* **8**, 1525–1534 (2017).
832 22. Adams, D. W., Wu, L. J., Czaplewski, L. G. & Errington, J. Multiple effects of benzamide antibiotics
833 on FtsZ function. *Mol. Microbiol.* **80**, 68–84 (2011).
834 23. Männik, J., Driessen, R., Galajda, P., Keymer, J. E. & Dekker, C. Bacterial growth and motility in
835 sub-micron constrictions. *Proc. Natl. Acad. Sci. U. S. A.* **106**, 14861–14866 (2009).
836 24. Yang, D., Jennings, A. D., Borrego, E., Retterer, S. T. & Männik, J. Analysis of factors limiting
837 bacterial growth in PDMS mother machine devices. *Front. Microbiol.* **9**, (2018).
838 25. McGorty, R., Kamiyama, D. & Huang, B. Active microscope stabilization in three dimensions using
839 image correlation. *Opt. Nanoscopy* **2**, 3 (2013).

840 26. Stokes, N. R. *et al.* Novel inhibitors of bacterial cytokinesis identified by a cell-based antibiotic
841 screening assay. *J. Biol. Chem.* **280**, 39709–39715 (2005).
842 27. Silber, N., Mayer, C., Matos de Opitz, C. L. & Sass, P. Antibiotic-induced degradation of FtsZ reveals
843 distinct stages of Bacillus subtilis FtsZ ring assembly and constriction. *bioRxiv* (2020).
844 28. Lu, C., Stricker, J. & Erickson, H. P. Site-specific mutations of FtsZ - Effects on GTPase and in vitro
845 assembly. *BMC Microbiol.* **1**, (2001).
846 29. Redick, S. D., Stricker, J., Briscoe, G. & Erickson, H. P. Mutants of FtsZ targeting the protofilament
847 interface: Effects on cell division and GTPase activity. *J. Bacteriol.* **187**, 2727–2736 (2005).
848 30. Lyu, Z., Coltharp, C., Yang, X. & Xiao, J. Influence of FtsZ GTPase activity and concentration on
849 nanoscale Z-ring structure in vivo revealed by three-dimensional Superresolution imaging.
850 *Biopolymers* **105**, 725–734 (2016).
851 31. Gamba, P., Veening, J.-W., Saunders, N. J., Hamoen, L. W. & Daniel, R. A. Two-Step Assembly
852 Dynamics of the Bacillus subtilis Divisome. *J. Bacteriol.* **191**, 4186–4194 (2009).
853 32. Grimm, J. B. *et al.* A general method to improve fluorophores for live-cell and single-molecule
854 microscopy. *Nat. Methods* **12**, 244–250 (2015).
855 33. Westfall, C. S. & Levin, P. A. Bacterial Cell Size: Multifactorial and Multifaceted. *Annu. Rev.*
856 *Microbiol.* **71**, 499–517 (2017).
857 34. Dajkovic, A., Pichoff, S., Lutkenhaus, J. & Wirtz, D. Cross-linking FtsZ polymers into coherent Z
858 rings. *Mol. Microbiol.* **78**, 651–668 (2010).
859 35. Caldas, P. *et al.* Cooperative ordering of treadmilling filaments in cytoskeletal networks of FtsZ
860 and its crosslinker ZapA. *Nat. Commun.* **10**, 5744 (2019).
861 36. Huecas, S. *et al.* Self-Organization of FtsZ Polymers in Solution Reveals Spacer Role of the
862 Disordered C-Terminal Tail. *Biophys. J.* **113**, 1831–1844 (2017).
863 37. Sundararajan, K. & Goley, E. D. The intrinsically disordered C-terminal linker of FtsZ regulates
864 protofilament dynamics and superstructure in vitro. *J. Biol. Chem.* **292**, 20509–20527 (2017).

865 38. Buske, P. J. & Levin, P. A. A flexible C-terminal linker is required for proper FtsZ assembly in vitro
866 and cytokinetic ring formation in vivo. *Mol. Microbiol.* **89**, 249–263 (2013).
867 39. Denk, J., Huber, L., Reithmann, E. & Frey, E. Active Curved Polymers Form Vortex Patterns on
868 Membranes. *Phys. Rev. Lett.* **116**, 178301 (2016).
869 40. Pasquina-Lemonche, L. *et al.* The architecture of the Gram-positive bacterial cell wall. *Nature* **582**,
870 294–297 (2020).
871 41. Lambert, A. *et al.* Constriction Rate Modulation Can Drive Cell Size Control and Homeostasis in C.
872 crescentus. *iScience* **4**, 180–189 (2018).
873 42. Harris, L. K. & Theriot, J. A. Relative Rates of Surface and Volume Synthesis Set Bacterial Cell Size.
874 *Cell* **165**, 1479–1492 (2016).
875 43. Sun, Y. & Garner, E. PrkC modulates MreB filament density and cellular growth rate by monitoring
876 cell wall precursors. *bioRxiv* 2020.08.28.272336 (2020) doi:10.1101/2020.08.28.272336.
877 44. Coltharp, C., Buss, J., Plumer, T. M. & Xiao, J. Defining the rate-limiting processes of bacterial
878 cytokinesis. *Proc. Natl. Acad. Sci.* 201514296 (2016) doi:10.1073/pnas.1514296113.
879 45. de Jong, I. G., Beilharz, K., Kuipers, O. P. & Veening, J.-W. Live Cell Imaging of Bacillus subtilis and
880 Streptococcus pneumoniae using Automated Time-lapse Microscopy. *J. Vis. Exp.* (2011)
881 doi:10.3791/3145.
882 46. Harwood, C. R. & Cutting, S. M. *Molecular biological methods for Bacillus*. (Wiley, 1990).
883 47. Koo, B.-M. *et al.* Construction and Analysis of Two Genome-Scale Deletion Libraries for Bacillus
884 subtilis. *Cell Syst.* **4**, 291–305.e7 (2017).
885 48. Ellefsen, K. L., Dynes, J. L. & Parker, I. Spinning-Spot Shadowless TIRF Microscopy. *PLOS ONE* **10**,
886 e0136055 (2015).
887 49. Thevenaz, P., Ruttimann, U. E. & Unser, M. A pyramid approach to subpixel registration based on
888 intensity. *IEEE Trans. Image Process.* **7**, 27–41 (1998).
889 50. Dos Santos Caldas, P. R., Radler, P., Sommer, C. M. & Loose, M. Computational analysis of filament
890 polymerization dynamics in cytoskeletal networks. *Methods Cell Biol.* (2020).

51. Eberly, D., Gardner, R., Morse, B., Pizer, S. & Scharlach, C. Ridges for image analysis. *J. Math. Imaging Vis.* **4**, 353–373 (1994).

52. Tinevez, J.-Y. *et al.* TrackMate: An open and extensible platform for single-particle tracking. *Methods* **115**, 80–90 (2017).

53. Ho, J., Tumkaya, T., Aryal, S., Choi, H. & Claridge-Chang, A. Moving beyond P values: data analysis with estimation graphics. *Nat. Methods* **16**, 565–566 (2019).

54. Killick, R., Fearnhead, P. & Eckley, I. A. Optimal Detection of Changepoints With a Linear Computational Cost. *J. Am. Stat. Assoc.* **107**, 1590–1598 (2012).